Exploring the environmental drivers of global terrestrial CO_2 fluxes inferred from OCO-2 and a geostatistical inverse model

Zichong Chen[1], Scot M. Miller[1], Junjie Liu[2], Daven K. Henze[3], Deborah N. Huntzinger[4], and Kelley C. Wells[5]

[1]Department of Environmental Health and Engineering, Johns Hopkins University, Baltimore, MD, USA; [2]Jet Propulsion Laboratory, California Institute of Technology, Pasadena, CA, USA.; [3]Department of Mechanical Engineering, University of Colorado Boulder, Boulder, CO, USA;[4]School of Earth & Sustainability, Northern Arizona University, Flagstaff, AZ, USA; [5]Department of Soil, Water, and Climate, University of Minnesota-Twin Cities, St. Paul, MN, USA

Correspondence:

Zichong Chen

Department of Environmental Health and Engineering

Johns Hopkins University

Baltimore, MD, USA

zchen74@jhu.edu

Key points:

(1) We adapt the geostatistical approach to satellite-based inverse problems.

(2) A combination of photosynthetically active radiation, air temperature and precipitation best describe variations in CO_2 fluxes in most biomes across the globe.

(3) The geostatistical approach yields flux totals that are consistent with an OCO-2 inverse modeling inter-comparison.

Abstract

The carbon cycle displays strong sensitivity to short term variations in environmental conditions, and it is key to understand how these variations are linked with variations in CO_2 fluxes. Previously, atmospheric observations of CO_2 have been sparse in many regions of the globe, making it challenging to evaluate these relationships. However, the OCO-2 satellite, launched in July 2014, provides new insight into global CO_2 fluxes, particularly in regions that were previously difficult to monitor. In this study, we combine OCO-2 observations with a geostatistical inverse model to explore data-driven relationships between inferred CO_2 flux patterns and environmental drivers. We further use year 2016 as an initial case study to explore the applicability of the geostatistical approach to large satellite-based inverse problems. We estimate daily, global CO_2 fluxes at the model grid scale and find that a combination of air temperature, daily precipitation, and photosynthetically active radiation (PAR) best describe patterns in CO_2 fluxes in most biomes across the globe. PAR is an adept predictor of fluxes across mid-to-high latitudes, whereas a combined set of daily air temperature and precipitation shows strong explanatory power across tropical biomes. However, we are unable to quantify a larger number of relationships between environmental drivers and CO_2 fluxes using OCO-2 due to the limited sensitivity of total column satellite observations to detailed surface processes. Overall, we estimate a global net biospheric flux of -1.73 ± 0.53 GtC in year 2016, in close agreement with recent inverse modeling studies using OCO-2 retrievals as observational constraints.

1. Introduction

The carbon cycle is closely linked with short term environmental variations, and it is critical to explore the connections between these variations and variability in CO_2 fluxes. However, surface atmospheric CO_2 observations in many regions outside of North America and Europe are sparse, making it difficult to constrain CO_2 fluxes or to investigate the sensitivity of the CO_2 fluxes to underlying environmental drivers across many broad regions of the globe (e.g., *Peylin et al*., 2013; *Crowell et al*., 2019). We define the term "environmental drivers" as any meteorological variables or characteristics of the physical environment that can be modeled or measured and may correlate with net ecosystem exchange (NEE). Across North America, dense, continuous atmospheric CO_2 observations from ground-based towers and aircraft make it possible to extensively study the relationships between CO_2 fluxes and these environmental drivers at regional and continental levels (e.g., *Peters et al.,* 2007; *Gourdji et al.,* 2012; *Fang and Michalak,* 2015; *Shiga et al*., 2018); by contrast, a paucity of *in situ* observations for many regions, including the tropics and the Southern Hemisphere, makes it difficult to conduct comparable studies in these regions.

CO_2-observing satellites, including GOSAT (*Kuze et al*., 2009), TanSat (*Yang et al*., 2018) and OCO-2/OCO-3 (*Crisp*, 2015; *Eldering et al*., 2019) observe CO_2 broadly across the globe and can provide new insight into CO_2 fluxes, particularly in regions that were previously difficult to monitor (e.g., the tropics and Southern Hemisphere). To date, observations from the OCO-2 satellite, launched in July 2014, have been used to constrain CO_2 flux variability at point source (e.g., *Nassar et al*., 2017), regional (e.g., *Liu et al*., 2017; *Chatterjee et al*., 2017; *Palmer et al*., 2019) and global scales (e.g., *Crowell et al*., 2019; *Miller et al*., 2018; *Wang et al*., 2019). The next challenge is to connect OCO-2 observations and estimated CO_2 fluxes with environmental drivers (e.g., *Liu et al*., 2017; *Chevallier et al*., 2018). Understanding this connection between fluxes and environmental drivers is critical for improving bottom-up or process-based flux models (e.g., *Huntzinger et al*., 2017).

A geostatistical inverse model (GIM) provides a unique lens to explore these connections. Specifically, a GIM does not prescribe or rely on a traditional prior flux model. The choice of prior fluxes in a classical inverse model is often subjective, and this choice can impact the posterior flux estimate (e.g., *Peylin et al.,* 2013; *Houweling et al*., 2015; *Phillip et al.,* 2019). For example, existing state-of-art terrestrial biosphere models (TBMs) provide divergent flux estimates at regional to global scales and display very different sensitivities to environmental drivers (e.g., *Huntzinger et al*., 2017). By contrast, a GIM can assimilate a wide range of environmental drivers, making it possible to evaluate data-driven relationship between these drivers and the CO_2 fluxes inferred from atmospheric observations (see Sect. 2). Existing GIM studies have investigated connections of CO_2 fluxes and environmental drivers for North America (*Gourdji et al*., 2010, 2012; *Commane et al*., 2017; *Shiga et al*. 2018) and the globe (*Gourdji et al*., 2008) using a variety of *in situ* CO_2 observations.

New satellite observations of CO_2 provide a novel opportunity to expand this analysis across the globe. However, the sheer number of observations from satellites like OCO-2 also present novel computational and statistical challenges for GIMs that were originally designed for far smaller *in situ* CO_2 datasets (e.g., *Miller et al*., 2019). To overcome this challenge, we combine the GIM with the adjoint of a global chemical transport model. Using this framework, we not only estimate daily global CO_2 fluxes at the model grid scale (4° latitude $\times$ 5° longitude) but also quantify posterior uncertainties in the estimated fluxes. The primary purpose of this study is to

couple a GIM to a global adjoint model and use this framework to evaluate the relationships between the environmental drivers and the CO_2 fluxes inferred from OCO-2. We focus on a single year (i.e., 2016) as an initial case study -- to explore the applicability of the geostatistical approach to large satellite-based inverse problems. We first describe the implementation of the GIM for OCO-2 observations; we then evaluate and discuss the results of this approach (e.g., inferred flux estimates and relationships with environmental drivers) using the 2016 case study.

2. Data and Methods

2.1 Approach overview

We design a framework that couples the GIM to a global adjoint model (version v35n of the GEOS-Chem adjoint, *Henze et al*., 2007) and explore the applicability of the geostatistical approach to inverse problems with a large number of flux grid boxes (i.e., ~1.2×10^6) and a large number of OCO-2 satellite observations (i.e., ~9×10^4). We use year 2016 as an initial case study, as there is better temporal coverage of good-quality data from OCO-2 throughout the entire year relative to years 2015 and 2017. For example, there are 7 week-long gaps in the OCO-2 data in year 2015 and a 1.5-month gap in the OCO-2 data in year 2017, whereas there are no such gaps in year 2016. This time period also overlaps with an OCO-2 inverse modeling inter-comparison (MIP) study, enabling direct comparison with those results (*Crowell et al*., 2019). We specifically estimate CO_2 fluxes for September 1, 2015 to December 31, 2016 but discard the first four months as a spin-up time period. We also offer up a wide range of environmental drivers and allow the GIM to select a subset that best predicts spatiotemporal patterns in CO_2 fluxes at the model grid scale, described in detail below (Sects. 2.2-2.4).

2.2. OCO-2 satellite observations

We utilize 10-s average X_{CO2} generated from version 9 of the satellite observations for the period from September 1, 2015 through the end of year 2016 (e.g., *Chevallier et al.,* 2019). We use both land nadir- and land glint-mode retrievals in the inverse model. Recent retrieval updates have eliminated biases that previously existed between land nadir and land glint observations (*O'Dell et al*., 2018). Moreover, *Miller and Michalak* (2020) evaluated the impact of these updated OCO-2 retrievals on the terrestrial CO_2 flux constraint in different regions of the globe; the authors

found that the inclusion of both land nadir and land glint retrievals yielded a stronger constraint on CO_2 fluxes relative to using only a single observation type.

2.3 Geostatistical inverse model

A GIM does not require an emission inventory or a bottom-up model as an initial guess of fluxes; instead, a GIM can leverage a wide range of environmental driver datasets to help predict spatial and temporal patterns in the CO_2 fluxes (e.g., *Gourdji et al*., 2008, 2012; *Shiga et al*., 2018). We further pair the GIM with a statistical approach known as model selection to objectively determine which set of drivers can best reproduce CO_2 observations from OCO-2. This setup makes it feasible to both estimate CO_2 fluxes and to explicitly quantify the relationships between the fluxes and the underlying environmental drivers.

The fluxes, as estimated by the GIM, consist of two components. First, the GIM will scale the environmental drivers to match patterns in the atmospheric observations, and this component of the flux estimate is referred to as the 'deterministic model'. Second, the GIM will model space-time patterns in the CO_2 fluxes that are implied by the atmospheric observations but not explained by any environmental drivers, and this component of the fluxes is referred to as the 'stochastic component'. The best flux estimate is a sum of the deterministic model and the stochastic component:

$$\boldsymbol{s} = \mathbf{X}\boldsymbol{\beta} + \boldsymbol{\zeta} \quad (1)$$

where $\boldsymbol{s}$ are $m \times 1$ unknown fluxes, $\mathbf{X}$ is a $m \times p$ matrix of environmental drivers (see Sect. 2.4), $\boldsymbol{\beta}$ are $p \times 1$ unknown scaling factors or drift coefficients. These coefficients quantify the relationships between each of the p environmental drivers (i.e., each column of $\mathbf{X}$) and the estimated CO_2 fluxes. The product of $\mathbf{X}$ and $\boldsymbol{\beta}$ is the deterministic model ($\mathbf{X}\boldsymbol{\beta}$). The stochastic component ($\boldsymbol{\zeta}$) is zero-mean with a pre-specified spatial and/or temporal correlation structure; it describes spatial and temporal patterns in the fluxes that are not captured by the deterministic model. For the setup here, the drift coefficient ($\boldsymbol{\beta}$) associated with each environmental driver is constant in space and time, while the stochastic component ($\boldsymbol{\zeta}$) varies at the model grid scale. We estimate both the fluxes ($\boldsymbol{s}$) and the drift coefficients ($\boldsymbol{\beta}$) by minimizing the GIM cost function (e.g., *Kitanidis and Vomvoris*, 1983; *Kitanidis*, 1995*; Michalak et al*., 2004):

$$L_{s,\beta} = \frac{1}{2}(\boldsymbol{z} - h(\boldsymbol{s}))^{\boldsymbol{T}}\mathbf{R}^{-1}(\boldsymbol{z} - h(\boldsymbol{s})) + \frac{1}{2}(\boldsymbol{s} - \mathbf{X}\boldsymbol{\beta})^{\boldsymbol{T}}\mathbf{Q}^{-1}(\boldsymbol{s} - \mathbf{X}\boldsymbol{\beta}) \quad (2)$$

The cost function includes two components: the first component indicates that the fluxes ($\boldsymbol{s}$), when run through an atmospheric model, $h(\boldsymbol{s})$, should match the observations ($\boldsymbol{z}$) to within a specific error tolerance ($\boldsymbol{z} - h(\boldsymbol{s})$) that is prescribed by the covariance matrix $\mathbf{R}$ ($n \times n$). $\mathbf{R}$ describes model-data mismatch errors, including errors from the atmospheric transport model and the OCO-2 retrievals, among other errors. The second component of Eq. 2 stipulates that the structure of the stochastic component ($\boldsymbol{s} - \mathbf{X}\boldsymbol{\beta}$) is described by the covariance matrix $\mathbf{Q}$ ($m \times m$). $\mathbf{Q}$, like $\mathbf{R}$, must be defined by the modeler before estimating the fluxes; it represents the variances and spatiotemporal covariances of the stochastic component. We estimate $\mathbf{Q}$ using a statistical approach known as Restricted Maximum Likelihood (RML; e.g., *Kitanidis*, 1997; *Gourdji et al*., 2012; *Miller et al*., 2016). $\mathbf{Q}$ includes both diagonal and off-diagonal elements; the latter decay with the separation time and distance between two model grid boxes. We construct $\mathbf{R}$ as a diagonal matrix with constant elements on the diagonal. Supporting Information Text S1 provides a detailed explanation of the approach used here to estimate the covariance matrix parameters.

After estimating the covariance matrix parameters, we then estimate the CO_2 fluxes by iteratively minimizing Eq. 2 using the Limited-memory Broyden-Fletcher-Goldfarb-Shanno algorithm (L-BFGS, *Liu and Nocedal*, 1989). We use this approach to simultaneously estimate both $\boldsymbol{s}$ and $\boldsymbol{\beta}$. *Miller et al* (2019) describe this iterative approach to minimize Eq. 2 in detail.

2.4 Auxiliary environmental drivers

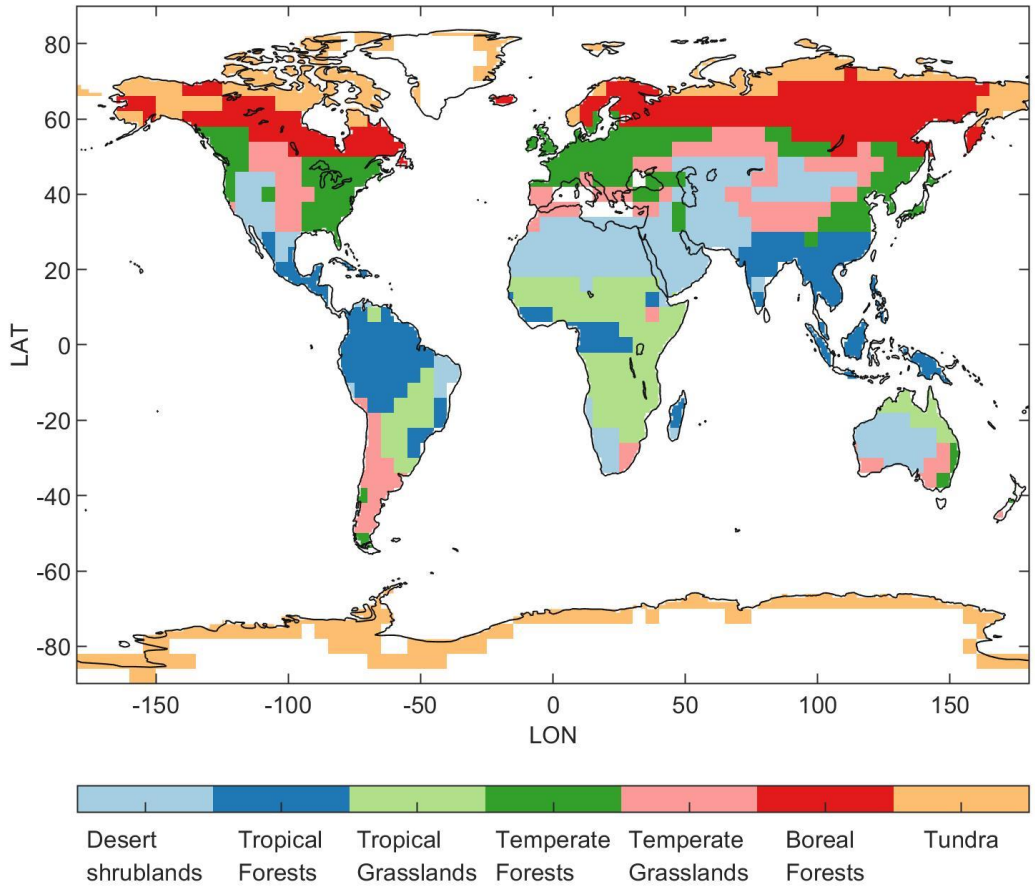

Figure 1. The seven biome-based regions aggregated from a world biome map in *Olsen et al* (2001).

We consider a wide range of environmental drivers (**X**). These are meteorological variables primarily related to heat, water, and radiation, available from NASA's Modern-Era Retrospective Analysis for Research and Applications, Version 2 (MERRA-2, *Rienecker et al*., 2011). Specifically, we consider daily 2-m air temperature, daily precipitation, 30-day average precipitation, photosynthetically active radiation (PAR), surface downwelling shortwave radiation, soil temperature at 10-cm depth, soil moisture at 10-cm depth, specific humidity, and relative humidity. We also include a non-linear function of 2-m air temperature as an environmental driver (refer to hereafter as scaled temperature). This function is from the Vegetation Photosynthesis and Respiration Model (VPRM, *Mahadevan et al*., 2008) and describes the non-linear relationship between temperature and photosynthesis (e.g., *Raich et al*. 1991, see Supporting Information Text S2).

Note that we do not include any remote sensing indices (e.g., solar-induced chlorophyll fluorescence (SIF) or leaf area index (LAI)) in the present study. Rather, the focus of this study is to explore environmental drivers of CO_2 fluxes, not remote sensing proxies for CO_2 fluxes.

We group the globe into seven biome-based regions and allow the GIM to use different environmental drivers in different biomes. The seven-biome map (Fig. 1) is derived from the biomes in *Olson et al* (2001), aggregated to form larger regions. As a result of this setup, each column of **X** includes a single environmental driver for a single biome. Therefore, each environmental driver is represented by a total of seven columns in **X**. Within each column, all elements are zeros except for elements that correspond to a single biome.

We also include several constant columns of ones in **X**. These columns are analogous to the intercept in a linear regression. Existing GIM studies always include one or more constant columns within **X** (e.g., *Gourdji et al.* 2008; *Gourdji et al*., 2012; *Miller et al*., 2016). In this study, we specifically use a total of seven constant columns, one for each biome. We also include a constant column for the ocean.

We further consider non-biospheric fluxes in the **X** matrix, including fossil fuel emissions from the Open-source Data Inventory for Anthropogenic CO_2 monthly fossil fuel emissions (ODIAC2016, *Oda et al*., 2018), climatological ocean fluxes from *Takahashi et al*. (2016), and biomass burning fluxes from the Global Fire Emissions Database (GFED) version 4.1 (*Randerson et al*., 2018). We only allocate a single column of **X** for fossil fuel, biomass burning, and ocean fluxes, respectively, because these fluxes are not the focus of this study.
In total, we consider a total of 81 columns for the **X** matrix: 8 constant columns of ones, 70 columns associated with environmental drivers, and 3 columns associated with anthropogenic, ocean, and biomass burning fluxes.

2.5 Model selection

We utilize a model selection framework to evaluate which subset of the environmental drivers (i.e., columns of **X**) best describe variations in CO_2 fluxes as inferred from the OCO-2 observations. The inclusion of additional environmental drivers or columns in **X** will always improve the model-data fit, but the inclusion of too many variables in **X** can yield an overfit of the OCO-2 observations or can yield unrealistic drift coefficients ($\boldsymbol{\beta}$) (e.g., *Zucchini*, 2000).

Instead of including all environmental drivers in **X**, we use model selection to decide which set of environmental drivers to include in **X**. In this study, we implement a type of model selection known as the Bayesian Information Criterion (BIC; *Schwarz*, 1978), which has been extensively used in recent GIM studies (e.g., *Gourdji et al*., 2012; *Miller et al.* 2013; *Fang and Michalak*, 2015). Using the BIC, we score different combinations of environmental drivers that could be included in **X** based on how well each combination reproduces the OCO-2 observations. We calculate these scores using the following equation for the implementation here (*Miller et al.* 2018*; Miller and Michalak,* 2020):

$$BIC = L + p\ln(n^*) \quad (3)$$

where L is log likelihood of a particular combination of environmental drivers (i.e., columns of **X**), p is the number of environmental drivers in this particular combination, and n^* is the effective number of independent observations. The first component (L) rewards combinations that are a better fit to the observations, whereas the second component in Eq. 3 ($p\ln(n^*)$) penalizes models with a greater number of columns to prevent overfitting. The best combination of environmental drivers for **X** is the combination that receives the lowest score (Supporting Information Text S3 and Table S2). We implement the BIC using a heuristic branch and bound algorithm (*Yadav et al*., 2013) to reduce computing time. *Miller et al* (2018) describes this model selection procedure in greater detail, including the specific setup and equations for the BIC.

2.6 Posterior uncertainties

In a GIM, the direct solution to calculate the posterior covariance matrix $\mathbf{V_s}$ (dimensions m x m) can be computed as (e.g., *Saibaba and Kitanidis*, 2014; *Miller et al.*, 2019):

$$\mathbf{V_s} = \mathbf{V_1} + \mathbf{V_2}\mathbf{V_3}\mathbf{V_2^T} \quad (4)$$

$$\mathbf{V_1} = (\mathbf{Q^{-1}} + \mathbf{H^T}(\mathbf{R^{-1}}\mathbf{H}))^{-1} \quad (5)$$

$$\mathbf{V_2} = \mathbf{V_1}\mathbf{Q^{-1}}\mathbf{X} \quad (6)$$

$$\mathbf{V_3} = (\mathbf{X^T}\mathbf{Q^{-1}}\mathbf{X} - (\mathbf{Q^{-1}}\mathbf{X})^T\mathbf{V_1}\mathbf{Q^{-1}}\mathbf{X})^{-1} \quad (7)$$

where the posterior error covariance matrix $\mathbf{V_s}$ is the sum of $\mathbf{V_1}$ and $\mathbf{V_2V_3V_2^T}$, and $\mathbf{H}$ is a n ×m matrix describing the footprint sensitivity of the observations ($\boldsymbol{z}$) to the fluxes ($\boldsymbol{s}$). Note that $\mathbf{V_1}$ is the posterior error covariance matrix in a classic Bayesian inverse model (e.g., *Rodgers,* 2000; *Brasseur and Jacob*, 2017). $\mathbf{V_2V_3V_2^T}$ accounts for the additional uncertainty in the fluxes due to the unknown drift coefficients ($\boldsymbol{\beta}$).

The calculations in Eq. 5 are not computationally feasible for most inverse problems with very large datasets; the matrix sum in $\mathbf{V_1}$ is often too large to invert, and we do not explicitly construct an $\mathbf{H}$ matrix or its transpose $\mathbf{H^T}$. Instead, we employ a low-rank approximation of $\mathbf{V_1}$ that circumvents these problems. Specifically, we approximate the matrices in $\mathbf{V_1}$ as a low rank update to $\mathbf{Q}$ using a limited number of eigenpairs (i.e., eigenvectors and eigenvalues). *Miller et al* (2019) and the Supporting Information Text S4 describe the uncertainty quantification in greater detail.

3. Results and Discussion

3.1 Connections between CO_2 fluxes and environmental drivers

Table 1. *Estimated drift coefficients (**β**) and associated uncertainties in **β** for environmental drivers selected using the BIC*

Biomes	Selected environmental drivers	Drift coefficients (**β**)	Uncertainties in **β**, with 95% confidence interval*
Boreal forests	PAR	-1.59	0.16
Temperate grasslands	Daily precipitation	-0.15	0.05
	PAR	-0.29	0.04
Temperate forests	Daily precipitation	-0.36	0.03
	PAR	-0.81	0.03
Tropical grasslands	Daily precipitation	-0.55	0.06
	Scaled temperature	-0.35	0.04
Tropical forests	Daily precipitation	-0.23	0.05
	PAR	0.27	0.05
	Scaled temperature	-0.04	0.02
Desert and shrublands	Daily precipitation	-0.27	0.03
	Scaled Temperature	-0.07	0.01

*Supporting Information Text S5 provides detail on the calculations of uncertainties in **β**.

A small number of environmental drivers can describe most spatiotemporal variability in CO_2 fluxes as estimated in the GIM. In this study, we define spatiotemporal variability as any spatial or temporal patterns in CO_2 fluxes that manifest at the daily, 4^o (latitude) × 5^o (longitude) resolutions of the GEOS-Chem model during the one-year study period (year 2016). The deterministic model accounts for ~89.6% of the variance in the estimated fluxes (Fig. 2a), and the stochastic component conversely accounts for only 10.4% of the flux variance (Fig. 2b).

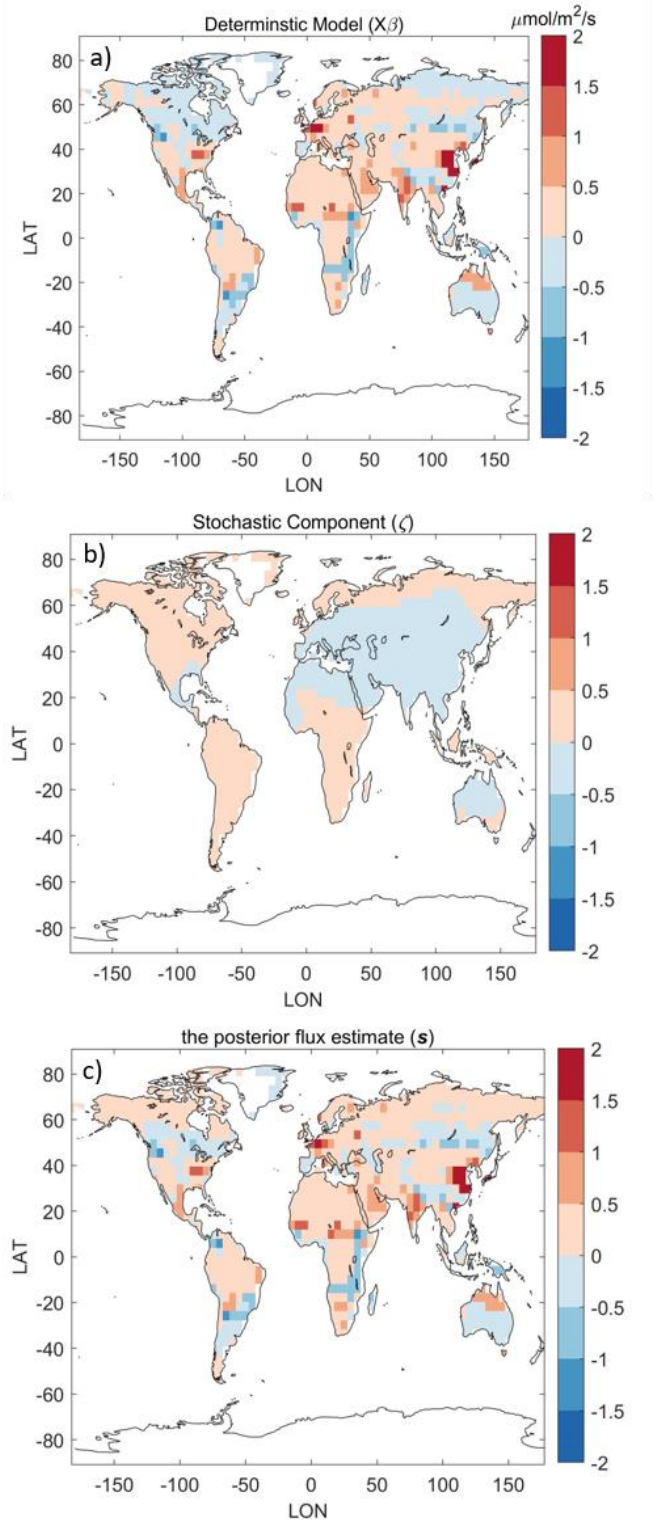

Figure 2. Estimated terrestrial fluxes from (a) the deterministic component ($\mathbf{X}\boldsymbol{\beta}$) and (b) the stochastic component ($\boldsymbol{\zeta}$). The sum of these two components

equals (c) the posterior flux estimates (***s***). Here the posterior flux estimates include contributions from all source types, including flux patterns that map onto fossil fuels from ODIAC2016.

A combination of PAR, daily temperature, and daily precipitation best describe patterns in CO_2 fluxes in most biomes across the globe (Table 1). PAR is an adept predictor of fluxes across mid-to-high latitudes, whereas a combined set of daily air temperature and daily precipitation are better predictors across tropical biomes.

The deterministic model also includes fossil fuel emissions from ODIAC2016 but not biomass burning fluxes from GFED or ocean fluxes from *Takahashi et al*., (2016). Fossil fuel emissions from ODIAC2016, when passed through the GEOS-Chem model, help describe enough variability in the OCO-2 observations to be selected using the BIC. By contrast, neither biomass burning fluxes from GFED nor ocean fluxes from *Takahashi et al*. (2016) help reproduce the OCO-2 observations more than the penalty term in the BIC, and these fluxes are therefore not selected using the BIC. Specifically, biomass burning and ocean fluxes may not have been selected for several reasons: either those fluxes are small relative to fossil fuel emissions and NEE, the land OCO-2 observations from 2016 are not sensitive to biomass burning and ocean fluxes, and/or the flux patterns in GFED and *Takahashi et al*., (2016) are not consistent with the OCO-2 observations. Instead, biomass burning and ocean fluxes are included within the stochastic component of the flux estimate.

Overall, we only select a limited number of environmental drivers (12 out of 70, ~18%) using model selection. Specifically, we never select more than 3 environmental drivers in any individual biome (Table 1). This result indicates two likely conclusions. First, a few simple linear relationships may adeptly describe flux variability at the scale and resolution of a global gridded atmospheric model, although the underlying leaf- and organism-level processes are admittedly more complex. Indeed, previous top-down studies (e.g., *Gourdji et al*., 2008, 2012; *Fang and Michalak*, 2015; *Shiga et al*., 2018) also found that simple linear relationships can effectively describe broad spatial and temporal patterns in CO_2 flux variability across North

335 America and across the globe. Such simple linear relationships allow for a straightforward
336 assessment of the explanatory power of environmental drivers, and make it possible to compare
337 these relationships inferred from atmospheric observations against the relationships used in
338 TBMs (e.g., *Huntzinger et al*., 2013; *Fang and Michalak*, 2015).

339 Second, additional environmental drivers, when run through an atmospheric transport model and
340 interpolated to the times and locations of OCO-2 observations, are not sufficiently unique to
341 parse out their differing relationships with CO_2 fluxes. Model selection ensures that we only
342 include environmental drivers that contribute unique information to the flux estimate and do not
343 overfit the OCO-2 observations. If multiple environmental drivers are highly correlated or
344 colinear, then the inclusion of more than one of these drivers will not contribute unique
345 information. As a result, we are unable to quantify a larger number of environmental driver
346 relationships using OCO-2. Fig. 3 illustrates an example of air temperature and PAR. In most of
347 the biomes, there is a weak correlation ($R < 0.4$; left column) between 2-m air temperature and
348 PAR; however, the correlation is much stronger ($R > 0.8$; right column) when these
349 environmental drivers are passed through an atmospheric model ($h(\mathbf{X})$). A larger number of
350 environmental drivers is not selected due to this high level of correlation or collinearity among
351 the columns in $h(\mathbf{X})$. This collinearity, not errors in the OCO-2 retrievals or atmospheric model,
352 appears to be a limiting factor in the model selection results.

353

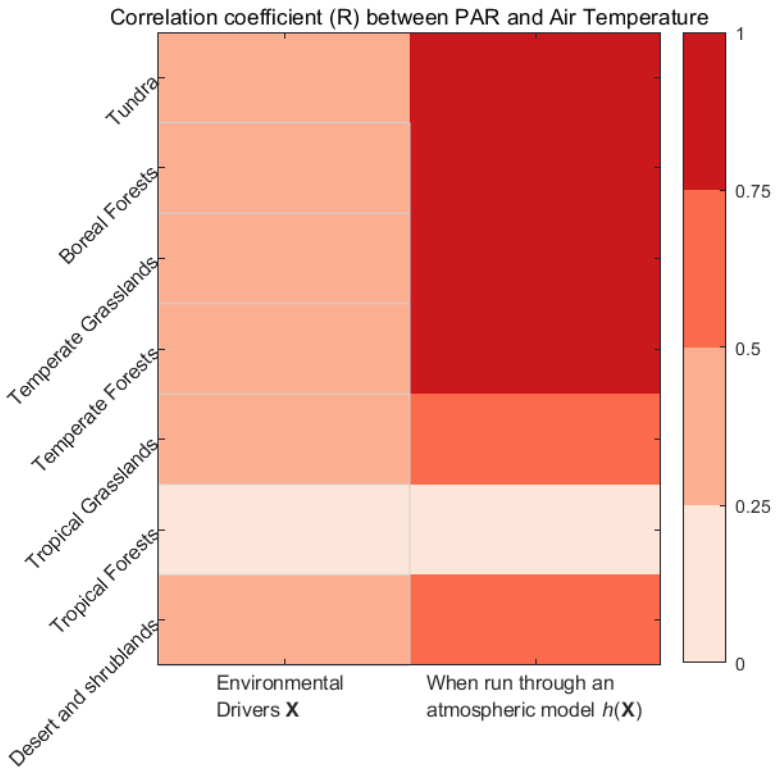

Figure 3. The correlation coefficient (R) between 2-m air temperature and PAR within different global biomes. The left panel shows correlations between air temperature and PAR from MERRA-2, re-gridded to the GEOS-Chem model grid; these environmental drivers are the columns of **X** (Eq. 1). The right panel displays the correlations between these variables after they have been passed through an atmospheric model, *h*(**X**). The correlation between 2-m air temperature and PAR is weak (R < 0.4) in most of the biomes; however, the correlation is much stronger (R > 0.8) when these environmental drivers are passed through an atmospheric model. The correlations among other pairs of environmental drivers show similar patterns.

354

355

356

3.1.1 PAR shows stronger explanatory power than temperature or precipitation in mid-to-high latitudes

PAR is selected for four biomes: temperature forests, temperate grasslands, boreal forests and tropical forests (Table 1). In the middle and high latitudes, PAR, rather than temperature or precipitation, appears to better reproduce seasonal patterns in CO_2 fluxes. This result reflects the fact that light availability is likely an important factor that drives CO_2 flux variability in mid-to-high latitudes (e.g., *Fang and Michalak*, 2015; *Baldocchi et al*., 2017). The $\boldsymbol{\beta}$ values for PAR indicate a strong to moderate negative correlation with estimated CO_2 fluxes, suggesting that an increase (or decrease) in PAR is associated with a decrease (or increase) in NEE, and an increase (or decrease) in carbon uptake; this $\boldsymbol{\beta}$ value is larger in boreal and temperate forests relative to grasslands, indicating a stronger relationship between PAR and net biosphere CO_2 fluxes in those biomes (Table 1; Fig. 4a).

Indeed, previous studies also indicate that PAR and similar environmental drivers (e.g., shortwave radiation) are closely associated with CO_2 fluxes. For example, a top-down study of North America (*Fang and Michalak*, 2015) found that shortwave radiation is more adept than other environmental variables in reproducing spatiotemporal variability of NEE, particularly across the growing season. Moreover, several site-level studies have reached parallel conclusions (e.g., *Mueller et al*., 2010; *Yadav et al*., 2010); these studies indicated that PAR is strongly correlated with photosynthesis, consistent with current mechanistic understandings of the light limitation on photosynthesis (e.g., *Gough et al*., 2007).

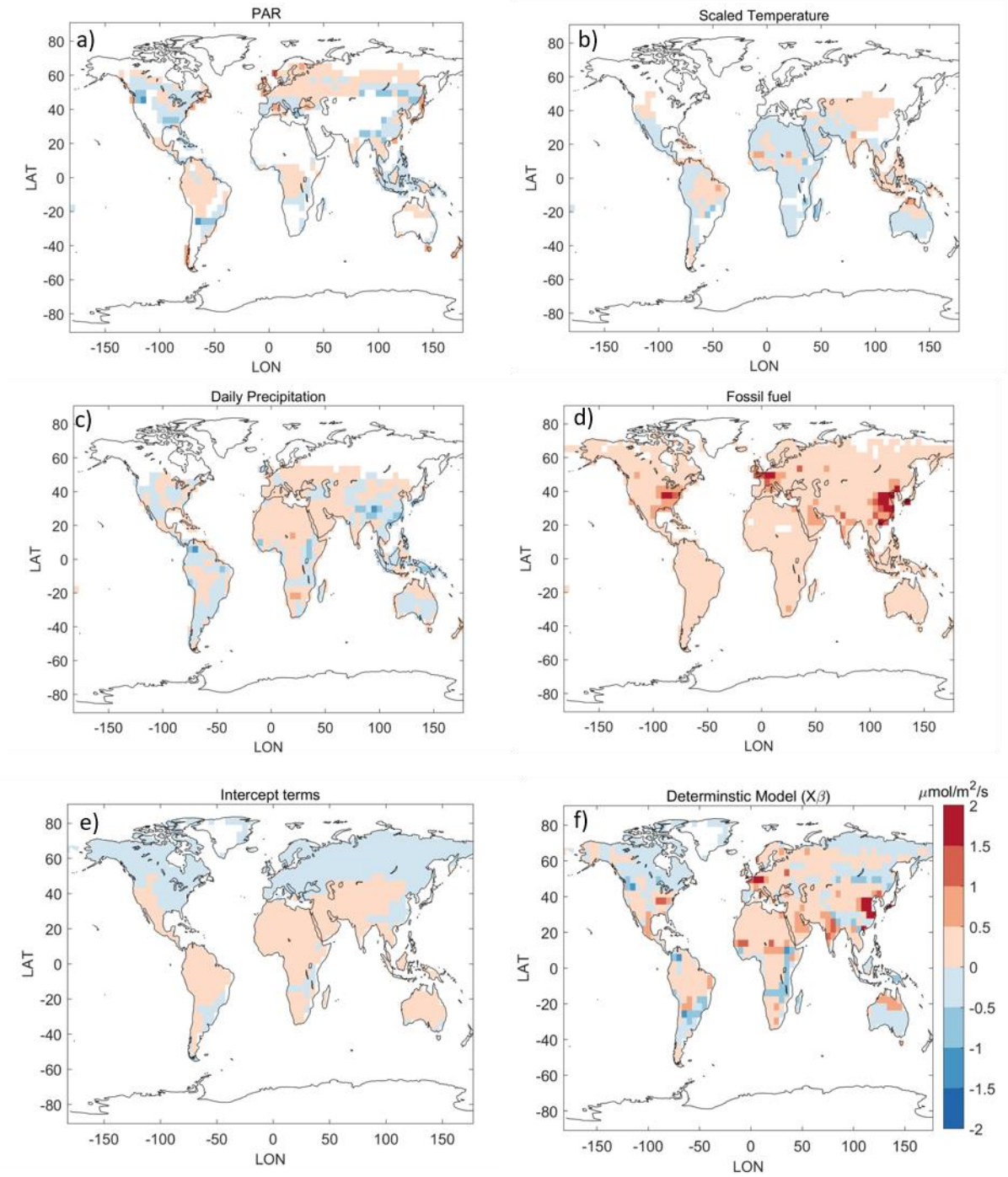

Figure 4. The contribution of different environmental drivers ($\mathbf{X}\boldsymbol{\beta}$) to estimated CO_2 fluxes from the GIM. The individual panels display the contribution of a) PAR, b) scaled temperature, c) daily precipitation, d) fossil fuel, e) the intercept terms, and f) the full deterministic model ($\mathbf{X}\boldsymbol{\beta}$). White colors in panels (a-c) reflect the fact that not all environmental drivers are selected in all biomes.

3.1.2 Drought is likely associated with flux variations across tropical forests

A composite of PAR, scaled temperature, and daily precipitation adeptly describe variability in CO_2 fluxes across tropical forests, as seen through the OCO-2 observations. PAR in tropical forests is usually a function of the presence or absence of clouds (e.g., *Baldocchi et al*., 2017; *Zeri et al*., 2014); cloudiness is also associated with rainfall. Therefore, low PAR over tropical forests is likely an indicator of cloud presence and rainfall. A positive β estimated for PAR suggests that a decrease in PAR, indicative of enhanced precipitation, is associated with increased carbon uptake. Furthermore, the negative β value assigned to scaled temperature (Supporting Information Text S2) implies that an increase in air temperature, which often exceeds optimal temperature over tropical forests, is associated with reduced carbon uptake.

Recent studies (e.g., *Jiménez-Muñoz et al*., 2016; *Liu et al*., 2017; *Palmer et al*., 2019) indicated that tropical droughts associated with the 2015-2016 El Niño events likely resulted in above average carbon release. Indeed, the combination of high values of PAR, high air temperature, and low precipitation may be a manifestation of these drought impacts.

Indeed, multiple lines of evidence indicate that drought is associated with diminished carbon uptake in tropical forests (e.g., *Philips et al*., 2009; *Brienen et al*., 2015; *Baccini et al*., 2017). For example, *Gatti et al* (2014) suggested that a suppression of photosynthesis during tropical drought may cause a reduction in carbon uptake. *Brienen et al* (2015) added that tropical drought is often associated with higher-than-normal temperature, which may further contribute to reducing gross primary production (GPP) and carbon uptake. Overall, this GIM study supports the conclusion that environmental conditions indicative of drought are associated with net carbon emissions from tropical forests.

3.1.3 CO_2 fluxes, as inferred from OCO-2, are closely correlated with temperature and precipitation in tropical grasslands

Temperature and precipitation closely correlate with variability in CO_2 fluxes across tropical grasslands. This result suggests that heat and water availability are likely associated with carbon fluxes across this biome.

A negative $\boldsymbol{\beta}$ value for precipitation indicates that an increase in precipitation is associated with an increase in carbon uptake, which is in line with current knowledge that water availability facilitates photosynthesis, especially in arid or semi-arid regions. In addition, a negative $\boldsymbol{\beta}$ value for scaled temperature (Supporting Information Text S2) indicates that an increase in air temperature is associated with a reduction in carbon uptake. Specifically, high temperatures in the tropics often exceed the optimal temperature for photosynthesis (e.g., *Baldocchi et al*., 2017), which can suppress GPP (e.g., *Doughty and Golden*, 2008). Overall, a combined set of air temperature and precipitation adeptly describes CO_2 flux variability in tropical grasslands, rendering it a net source in year 2016.

3.2 **Estimated biospheric flux totals for different global regions**

We estimate a global terrestrial biospheric CO_2 budget of -1.73 ± 0.53 GtC (Uncertainties listed are the 95% confidence interval. Supporting Information Text S5 provides detail on the posterior uncertainty estimate for biospheric fluxes.). Among the seven biomes, middle to high latitudes (primarily temperate, boreal and tundra biomes) act as a significant carbon sink; tropical biomes are a net source; desert and shrubland regions play a small, neutral role (Table 2). Note that we subtract flux patterns that map onto fossil fuels ($\mathbf{X}\boldsymbol{\beta}$, Fig. 4d) from the posterior flux estimate ($\boldsymbol{s}$, Fig. 2c) to obtain an estimate for biospheric fluxes (including terrestrial NEE and biomass burning fluxes). We estimate a $\boldsymbol{\beta}$ value of 1.09 ± 0.05 (95% confidence interval) for the fossil fuel emissions from ODIAC2016, indicating that the overall global magnitude of ODIAC2016 is consistent with OCO-2 observations. We therefore assume that ODIAC2016 is a reasonable global estimate for fossil fuel emissions.

Table 2. *Biospheric CO_2 flux totals estimated for different global biomes*

biomes	Tundra	Boreal forests	Temperate grasslands	Temperate forests	Tropical grasslands	Tropical forests	Deserts/shrublands
Flux budget (Gt C yr^{-1}, with 95% confidence interval)	-0.01 ± 0.31	-0.62 ± 0.25	-1.71 ± 0.43	-1.78 ± 0.27	1.21 ± 0.44	1.16 ± 0.76	0.02 ± 0.30

These flux totals are broadly consistent with a recent MIP of different inverse models that assimilate OCO-2 observations (*Crowell et al*., 2019). The inverse modeling teams that participated in the MIP employed different transport models, inverse modeling approaches, and prior flux assumptions. The total global terrestrial biospheric flux, averaged across all models, was -1.4 ± 0.7 GtC for the year of 2016. The MIP fluxes assimilate v7 of land nadir-mode X_{CO2} retrievals; unlike this study in which we use v9 of land nadir- and glint-mode retrievals. In spite of this difference, the averaged global flux from the MIP study and the estimate reported here are very similar.

In order to provide an additional comparison with the MIP results, we group the estimated fluxes into TRANSCOM land regions (*Gurney et al*., 2002). We split the classic TRANSCOM regions at the Equator to avoid regions that encompass parts of both the northern and southern hemisphere, as in *Crowell et al* (2019). In most of the regions, the fluxes estimated using the GIM are very similar to those reported in the MIP (Fig. 5); however, the fluxes estimated here are significantly different in a limited number of regions (e.g., tropical Australia and northern tropical Africa), a possible reflection of differences between the v9 and v7 OCO-2 retrievals (*O'Dell et al*., 2018; *Miller et al*., 2019). For example, we estimate a smaller CO_2 source for northern tropical Africa relative to the MIP study. However, previous studies (e.g., *Wang et al*., 2019) indicated that existing satellite-based estimates of CO_2 fluxes for this region may be too high. OCO-2 collects far more observations across northern Africa during the dry season than the wet season due to persistent cloudiness in the wet season, and existing studies have postulated that this difference in data availability may be to blame for a high bias in CO_2 fluxes estimated from OCO-2 (*Crowell et al*. 2019; *Wang et al*. 2019).

The fluxes estimated here are also broadly consistent with aircraft-based CO_2 observations, a topic discussed in the Supporting Information Text S6.

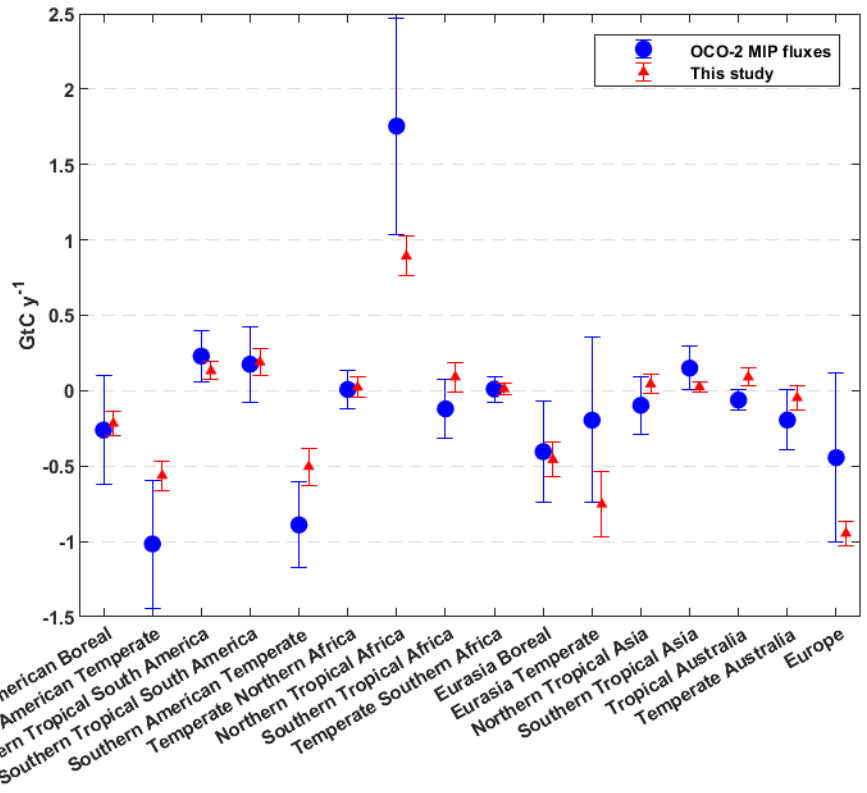

Figure 5. Comparison of regional (TRANSCOM-based) biospheric flux estimates in this study (red) and the MIP study (blue).

3.3 Estimated posterior uncertainties

The posterior uncertainties for individual biomes range from 0.25 to 0.76 GtC yr^{-1}. Estimated fluxes for tropical forests have higher uncertainties than any other biome (0.76 GtC yr^{-1}), likely a consequence of poor observational coverage due to persistent cloudiness. By contrast, a large number of good-quality OCO-2 retrievals provides robust constraints over temperate forests, yielding a small posterior uncertainty (0.27 GtC yr^{-1}) in the estimated flux.

It is important to note that the posterior uncertainties calculated in most classical Bayesian or geostatistical inverse models account for many but not all possible sources of uncertainty. For example, the posterior uncertainties presented here account for the sparsity of the OCO-2 observations, random observational or atmospheric transport errors, and uncertainties due to uncertain drift coefficients ($\boldsymbol{\beta}$) (e.g., *Kitanidis and Vomvoris*, 1983; *Michalak et al*., 2004).

However, these calculations do not fully account for bias-type errors: regional- or continental-scale biases in the OCO-2 observations, biases in modeled atmospheric convection (e.g., *Basu et al.*, 2018; *Schuh et al*., 2019), or biases in modeled interhemispheric transport, among other possible biases. Most classical Bayesian and geostatistical inverse models assume that the observational or model errors are Gaussian with a mean of zero (e.g., *Kitanidis and Vomvoris.* 1983; *Michalak et al*., 2004; *Tarantola*, 2005), making it challenging to account for the types of biases listed above. As a result, the posterior uncertainties estimated in this study are typically smaller than the range of flux estimates produced from the recent MIP study (Fig. 5; *Crowell et al*., 2019).

4. Conclusions

In this study, we couple a GIM to a global adjoint model and evaluate the data-driven relationships between environmental drivers and CO_2 fluxes inferred from OCO-2. Using year 2016 as an initial case study, we explore the applicability of the geostatistical approach to large satellite-based inverse problems. We find that

(1) A combination of air temperature, daily precipitation, and PAR best describe patterns in CO_2 fluxes in most biomes across the globe;

(2) PAR is an adept predictor of fluxes across mid-to-high latitudes, whereas a combination of daily air temperature and daily precipitation shows strong explanatory power across tropical biomes;

(3) A larger number of environmental driver datasets is not selected because they are not sufficiently unique to parse out their differing relationships with CO_2 fluxes using OCO-2. This high collinearity, not errors in the OCO-2 retrievals or atmospheric model, appears to be a limiting factor;

(4) We estimate a global terrestrial biospheric budget of -1.73 ± 0.53 GtC in year 2016, in close agreement with recent inverse modeling studies that use OCO-2 retrievals as observational constraints.

Acknowledgements

We thank David Baker and Andrew Jacobson for their help with the OCO-2 retrievals and the NASA MIP products. We also thank Colm Sweeny and Kathryn McKain for their help with aircraft datasets from the NOAA/ESRL Global Greenhouse Gas Reference Network. Financial support for this research has been provided by NASA ROSES grant no. 80NSSC18K0976. All modeling and analysis was performed on the NASA Pleiades Supercomputer.

Data availability

The version 9 of 10-s average OCO-2 retrievals are available at ftp://ftp.cira.colostate.edu/ftp/BAKER/; data information of the OCO-2 MIP is available at https://www.esrl.noaa.gov/gmd/ccgg/OCO2/; data information of the ObsPack data product is available at *http://www.esrl.noaa.gov/gmd/ccgg/obspack/*.

References

Baccini, A., Walker, W., Carvalho, L., Farina, M., & Houghton, R. A. (2019). Response to Comment on "Tropical forests are a net carbon source based on aboveground measurements of gain and loss." *Science*, *363*(6423), 230–234. https://doi.org/10.1126/science.aat1205

Baldocchi, D., Chu, H., & Reichstein, M. (2018). Inter-annual variability of net and gross ecosystem carbon fluxes: A review. *Agricultural and Forest Meteorology*, *249*(November 2016), 520–533. https://doi.org/10.1016/j.agrformet.2017.05.015

Basu, S., Baker, D. F., Chevallier, F., Patra, P. K., Liu, J., & Miller, J. B. (2018). The impact of transport model differences on CO 2 surface flux estimates from OCO-2 retrievals of column average CO 2. *Atmospheric Chemistry and Physics*, *18*(10), 7189-7215.

Brasseur, G. P. and Jacob, D. J. (2017). Modeling of Atmospheric Chemistry, chap. 11, Cambridge University Press, Cambridge, https://doi.org/10.1017/9781316544754

Brienen, R. J. W., Phillips, O. L., Feldpausch, T. R., Gloor, E., Baker, T. R., Lloyd, J., et al. (2015). Long-term decline of the Amazon carbon sink. *Nature*, *519*(7543), 344–348. https://doi.org/10.1038/nature14283

Chatterjee, A., Gierach, M. M., Sutton, A. J., Feely, R. A., Crisp, D., Eldering, A., et al. (2017). Influence of El Niño on atmospheric CO2 over the tropical Pacific Ocean: Findings from NASA's OCO-2 mission. *Science*, *358*(6360). https://doi.org/10.1126/science.aam5776

Commane, R., Lindaas, J., Benmergui, J., Luus, K. A., Chang, R. Y. W., Daube, B. C., et al. (2017). Carbon dioxide sources from Alaska driven by increasing early winter respiration from Arctic tundra. *Proceedings of the National Academy of Sciences of the United States of America*, *114*(21), 5361–5366. https://doi.org/10.1073/pnas.1618567114

Crisp, D. (2015). Measuring atmospheric carbon dioxide from space with the Orbiting Carbon Observatory-2 (OCO-2). *Earth Observing Systems XX*, *9607*(September 2015), 960702. https://doi.org/10.1117/12.2187291

Crowell, S., Baker, D., Schuh, A., Basu, S., Jacobson, A. R., Chevallier, F., Liu, J., Deng, F., Feng, L., McKain, K., Chatterjee, A., Miller, J. B., Stephens, B. B., Eldering, A., Crisp, D., Schimel, D., Nassar, R., O'Dell, C. W., Oda, T., Sweeney, C., Palmer, P. I., and Jones, D. B. A.: The 2015–2016 carbon cycle as seen from OCO-2 and the global in situ network, Atmos. Chem. Phys., 19, 9797–9831, https://doi.org/10.5194/acp-19-9797-2019, 2019. https://doi.org/10.5194/acp-2019-87

Chevallier, F. (2018). Comment on "Contrasting carbon cycle responses of the tropical continents to the 2015–2016 El Niño". *Science*, *362*(6418), https://doi.org/10.1126/science.aaar5432

Chevallier, F., Remaud, M., O'Dell, C. W., Baker, D., Peylin, P., & Cozic, A. (2019). Objective evaluation of surface-and satellite-driven CO2 atmospheric inversions. *Atmospheric Chemistry and Physics Discussions*, https://doi.org/10.5194/acp-2019-213

Eldering, A., Taylor, T. E., O'Dell, C. W., & Pavlick, R. (2019). The OCO-3 mission:

Measurement objectives and expected performance based on 1 year of simulated data. *Atmospheric Measurement Techniques*, *12*(4), 2341–2370. https://doi.org/10.5194/amt-12-2341-2019

Fang, Y., & Michalak, A. M. (2015). Atmospheric observations inform CO2 flux responses to enviroclimatic drivers. *Global Biogeochemical Cycles*, *29*(5), 555-566. https://doi.org/10.1002/2014/GB005034

Gatti, L. V., Gloor, M., Miller, J. B., Doughty, C. E., Malhi, Y., Domingues, L. G., et al. (2014). Drought sensitivity of Amazonian carbon balance revealed by atmospheric measurements. *Nature*, *506*(7486), 76–80. https://doi.org/10.1038/nature12957

Gough, C. M., C. S. Vogel, C. Kazanski, L. Nagel, C. E. Flower, and P. S. Curtis (2007), Coarse woody debris and the carbon balance of a north temperate forest, *For. Ecol. Manage.*, **244**, 60–67, doi:10.1016/j.foreco.2007.03.039

Gourdji, Sharon M., Mueller, K. L., Schaefer, K., & Michalak, A. M. (2008). Global monthly averaged CO 2 fluxes recovered using a geostatistical inverse modeling approach: 2. Results including auxiliary environmental data . *Journal of Geophysical Research*, *113*(D21), 1–15. https://doi.org/10.1029/2007jd009733

Gourdji, S. M., Hirsch, A. I., Mueller, K. L., Yadav, V., Andrews, A. E., & Michalak, A. M. (2010). Regional-scale geostatistical inverse modeling of North American CO 2 fluxes: A synthetic data study. *Atmospheric Chemistry and Physics*, *10*(13), 6151–6167. https://doi.org/10.5194/acp-10-6151-2010

Gourdji, S. M., et al. (2012), North American CO2 exchange: Inter-comparison of modeled estimates with results from a fine-scale atmospheric inversion, *Biogeosciences*, *9*(1), 457–475, https://doi.org/10.5194/bg-9-457-2012.

Houweling, S., Baker, D., Basu, S., Boesch, H., Butz, A., Chevallier, F., et al. (2015). An intercomparison of inversemodels for estimating sources and sinks of CO2 using GOSAT measurements. *Journal of Geophysical Research*, *120*(10), 5253–5266. https://doi.org/10.1002/2014JD022962

Huntzinger, D. N., Schwalm, C., Michalak, A. M., Schaefer, K., King, A. W., Wei, Y., et al. (2013). The North American carbon program multi-scale synthesis and terrestrial model intercomparison project - Part 1: Overview and experimental design. *Geoscientific Model Development*, *6*(6), 2121–2133. https://doi.org/10.5194/gmd-6-2121-2013

Huntzinger, D. N., Michalak, A. M., Schwalm, C., Ciais, P., King, A. W., Fang, Y., et al. (2017). Uncertainty in the response of terrestrial carbon sink to environmental drivers undermines carbon-climate feedback predictions. *Scientific Reports*, *7*(1), 1–8. https://doi.org/10.1038/s41598-017-03818-2

Jiménez-Muñoz, J. C., Mattar, C., Barichivich, J., Santamaría-Artigas, A., Takahashi, K., Malhi, Y., ... & Van Der Schrier, G. (2016). Record-breaking warming and extreme drought in the Amazon rainforest during the course of El Niño 2015–2016. *Scientific reports*, *6*, 33130. https://doi.org/ 10.1038/srep33130

Kitanidis, P. K., & Vomvoris, E. G. (1983). A geostatistical approach to the inverse problem in

groundwater modeling (steady state) and one-dimensional simulations. *Water Resources Research*, *19*(3), 677-690

Kitanidis, P. (1997). Introduction to Geostatistics: Applications in Hydrogeology, Stanford-Cambridge program, Cambridge University Press, Cambridge

Kuze, A., Suto, H., Nakajima, M., & Hamazaki, T. (2009). Thermal and near infrared sensor for carbon observation Fourier-transform spectrometer on the Greenhouse Gases Observing Satellite for greenhouse gases monitoring. *Applied Optics*, *48*(35), 6716–6733. https://doi.org/10.1364/AO.48.006716

Liu, D. C., & Nocedal, J. (1989). On the limited memory BFGS method for large scale optimization. *Mathematical programming*, *45*(1-3), 503-528.

Liu, J., Bowman, K. W., Schimel, D. S., Parazoo, N. C., Jiang, Z., Lee, M., ... & O'Dell, C. W. (2017) Contrasting carbon cycle responses of the tropical continents to the 2015–2016 El Niño. *Science*, *358*, 191. HTTPS://DOI.ORG/ 10.1126/science.aam5690

Mahadevan, P., Wofsy, S. C., Matross, D. M., Xiao, X., Dunn, A. L., Lin, J. C., ... & Gottlieb, E. W. (2008). A satellite-based biosphere parameterization for net ecosystem CO2 exchange: Vegetation Photosynthesis and Respiration Model (VPRM). *Global Biogeochemical Cycles*, *22*(2). https://doi.org/10.1029/2006GB002735

Michalak, A. M., Bruhwiler, L., & Tans, P. P. (2004). A geostatistical approach to surface flux estimation of atmospheric trace gases. *Journal of Geophysical Research D: Atmospheres*, *109*(14), 1–19. https://doi.org/10.1029/2003JD004422

Miller, S. M. and Michalak, A. M. (2020): The impact of improved satellite retrievals on estimates of biospheric carbon balance, Atmos. Chem. Phys., 20, 323–331, https://doi.org/10.5194/acp-20-323-2020. https://doi.org/10.5194/acp-20-323-2020

Miller, S. M., Michalak, A. M., Yadav, V., & Tadié, J. M. (2018). Characterizing biospheric carbon balance using CO2 observations from the OCO-2 satellite. *Atmospheric Chemistry and Physics*, *18*(9), 6785–6799. https://doi.org/10.5194/acp-18-6785-2018

Miller, S. M., Miller, C. E., Commane, R., Chang, R. Y. W., Dinardo, S. J., Henderson, J. M., et al. (2016). A multiyear estimate of methane fluxes in Alaska from CARVE atmospheric observations. *Global Biogeochemical Cycles*, *30*(10), 1441–1453. https://doi.org/10.1002/2016GB005419

Miller, S. M., Saibaba, A. K., Trudeau, M. E., & Andrews, A. E. (2019). Geostatistical inverse modeling with very large datasets : an example from the OCO-2 satellite. *Geoscientific Model Development*, https://doi.org/10.5194/gmd-2019-185

Miller, S. M., Wofsy, S. C., Michalak, A. M., Kort, E. A., Andrews, A. E., Biraud, S. C., ... & Miller, B. R. (2013). Anthropogenic emissions of methane in the United States. *Proceedings of the National Academy of Sciences*, *110*(50), 20018-20022. https://doi.org/10.1073/pnas.1314392110

Mueller, K. L., Yadav, V., Curtis, P. S., Vogel, C., & Michalak, A. M. (2010). Attributing the variability of eddy-covariance CO2 flux measurements across temporal scales using

geostatistical regression for a mixed northern hardwood forest. *Global Biogeochemical Cycles*, *24*(3). https://doi.org/10.1029/2009GB003642

Nassar, R., Hill, T. G., McLinden, C. A., Wunch, D., Jones, D. B. A., & Crisp, D. (2017). Quantifying CO2 Emissions From Individual Power Plants From Space. *Geophysical Research Letters*, *44*(19), 10,045-10,053. https://doi.org/10.1002/2017GL074702

O'Dell, C. W., Eldering, A., Wennberg, P. O., Crisp, D., Gunson, M. R., Fisher, B., et al. (2018). Improved retrievals of carbon dioxide from Orbiting Carbon Observatory-2 with the version 8 ACOS algorithm. *Atmospheric Measurement Techniques*, *11*(12), 6539–6576. https://doi.org/10.5194/amt-11-6539-2018

Oliphant, A., C. Susan, B. Grimmond, H. P. Schmid, and C. A. Wayson (2006), Local-scale heterogeneity of photosynthetically active radiation (PAR), absorbed PAR and net radiation as a function of topography, sky conditions and leaf area index, *Remote Sens. Environ.*, 103(3), 324–337, doi:10.1016/j.rse.2005.09.021.

Olson, D. M., Dinerstein, E., Wikramanayake, E. D., Burgess, N. D., Powell, G. V. N., Underwood, E. C., et al. (2001). Terrestrial Ecoregions of the World: A New Map of Life on Earth. *BioScience*, 51(11), 933. https://doi.org/10.1641/0006-3568(2001)051[0933:teotwa]2.0.co;2

Palmer, P. I., Feng, L., Baker, D., Chevallier, F., Bösch, H., & Somkuti, P. (2019). Net carbon emissions from African biosphere dominate pan-tropical atmospheric CO2 signal. *Nature Communications*, *10*(1), 3344. https://doi.org/10.1038/s41467-019-11097-w

Peters, W., Jacobson, A. R., Sweeney, C., Andrews, A. E., Conway, T. J., Masarie, K., et al. (2007). An atmospheric perspective on North American carbon dioxide exchange: CarbonTracker. *Proceedings of the National Academy of Sciences of the United States of America*, *104*(48), 18925–18930. https://doi.org/10.1073/pnas.0708986104

Peylin, P., Law, R. M., Gurney, K. R., Chevallier, F., Jacobson, A. R., Maki, T., et al. (2013). Global atmospheric carbon budget: Results from an ensemble of atmospheric CO 2 inversions. *Biogeosciences*, *10*(10), 6699–6720. https://doi.org/10.5194/bg-10-6699-2013

Phillips, O. L., Aragão, L. E., Lewis, S. L., Fisher, J. B., Lloyd, J., López-González, G., ... & Van Der Heijden, G. (2009). Drought sensitivity of the Amazon rainforest. *Science*, *323*(5919), 1344-1347. https://doi.org/10.1126/science.1164033

Raich, J. W. (1991). Potential net primary productivity in South America: application of a global model. *Ecological Applications*, *1*(4), 399–429. https://doi.org/10.2307/1941899

Randerson, J.T., G.R. van der Werf, L. Giglio, G.J. Collatz, and P.S. Kasibhatla. (2018). Global Fire Emissions Database, Version 4.1 (GFEDv4). ORNL DAAC, Oak Ridge, Tennessee, USA. https://doi.org/10.3334/ORNLDAAC/1293

Rodgers, C. D. (2000). *Inverse methods for atmospheric sounding: theory and practice* (Vol. 2). World scientific.

Schuh, A. E., Jacobson, A. R., Basu, S., Weir, B., Baker, D., Bowman, K., ... & Denning, S. (2019). Quantifying the impact of atmospheric transport uncertainty on CO2 surface flux

687 estimates. *Global Biogeochemical Cycles*, *33*(4), 484-500.
688 https://doi.org/10.1029/2018GB006086

689 Schwarz, G.: Estimating the dimension of a model, *Ann. Stat*., 6, 461–464, available at:
690 http://www.jstor.org/stable/2958889, 1978

691 Shiga, Y. P., Michalak, A. M., Fang, Y., Schaefer, K., Andrews, A. E., Huntzinger, D.
692 H., ... & Wei, Y. (2018). Forests dominate the interannual variability of the North
693 American carbon sink. *Environmental Research Letters*, *13*(8), 084015.
694 https://doi.org/10.1088/1748-9326/aad505
695 Takahashi, T., Sutherland, S., and Kozyr, A. (2016). Global Ocean Surface Water Partial
696 Pressure of CO2 Database: Measurements Performed During 1957–2015 (Version
697 2015), ORNL/CDIAC-160, NDP-088(V2015), Oak Ridge National Laboratory, U.S.
698 Department of Energy, Oak Ridge, Tennesee, http://doi.org/10.3334/CDIAC/OTG.ND
699 P088(V2015)
700
701 Tarantola, A. (2005). Inverse problem theory and methods for model parameter estimation (Vol.
702 89). *SIAM*.
703

704 Wang, H., Jiang, F., Wang, J., Ju, W., & Chen, J. M. (2019). Terrestrial ecosystem carbon flux
705 estimated using GOSAT and OCO-2 XCO 2 retrievals . *Atmospheric Chemistry and*
706 *Physics*, *19*(18), 12067–12082. https://doi.org/10.5194/acp-19-12067-2019

707 Yadav, V., Mueller, K. L., Dragoni, D., & Michalak, A. M. (2010). A geostatistical synthesis
708 study of factors affecting gross primary productivity in various ecosystems of North
709 America. *Biogeosciences*, *7*(9), 2655-2671. https://www.biogeosciences.net/7/2655/2010/

710 Yadav, V., Mueller, K. L., & Michalak, A. M. (2013). A backward elimination discrete
711 optimization algorithm for model selection in spatio-temporal regression models.
712 *Environmental Modelling and Software*, *42*, 88–98.
713 https://doi.org/10.1016/j.envsoft.2012.12.009

714 Yang, D., Liu, Y., Cai, Z., Chen, X., Yao, L., & Lu, D. (2018). First Global Carbon Dioxide
715 Maps Produced from TanSat Measurements. *Advances in Atmospheric Sciences*, *35*(6),
716 621–623. https://doi.org/10.1007/s00376-018-7312-6

717 Zeri, M., Sá, L. D. A., Manzi, A. O., Araú, A. C., Aguiar, R. G., Von Randow, C., et al. (2014).
718 Variability of carbon and water fluxes following climate extremes over a tropical forest in
719 southwestern amazonia. *PLoS ONE*, *9*(2). https://doi.org/10.1371/journal.pone.0088130

720 Zucchini, W. (2000). An introduction to model selection. *Journal of mathematical*
721 *psychology*, *44*(1), 41-61.

722

723